Modeling of dust-particle behavior for different materials in plasmas

著者	Tanaka Yasunori, Pigarov A. Yu., Smirnov R.D., Krasheninnikov S.I., Ohno N., Uesugi Yoshihiko
journal or publication title	Physics of Plasmas
volume	14
number	5
year	2007-01-01
URL	http://hdl.handle.net/2297/6750

doi: 10.1063/1.2722274

PHYSICS OF PLASMAS **14**, 052504 (2007)

Modeling of dust-particle behavior for different materials in plasmas

Y. Tanaka[a)]
Division of Electrical Engineering and Computer Science, Kanazawa University, Kakuma, Kanazawa 920-1192, Japan

A. Yu. Pigarov, R. D. Smirnov, and S. I. Krasheninnikov
Department of Mechanical and Aerospace Engineering, University of California at San Diego, La Jolla, California 92093

N. Ohno
EcoTopia Science Institute, Nagoya University, Furo-cho 464-8601, Japan

Y. Uesugi
Department of Electrical and Electronic Engineering, Kanazawa University, Kakuma, Kanazawa 920-1192, Japan

(Received 22 January 2007; accepted 12 March 2007; published online 11 May 2007)

The behavior of dust particles made of different fusion-related materials (Li, Be, B, C, Fe, Mo, or W) in tokamak plasmas is simulated using the dust transport code DUSTT [A. Pigarov *et al.*, Phys. Plasmas **12**, 122508 (2005)]. The dependencies of the characteristic lifetime of dust particles on plasma parameters are compared for the different dust materials. The dynamics of dust particles in the tokamak edge plasma is studied and the effects of dust material on the acceleration, heating, and evaporation/sublimation of particles are analyzed. © *2007 American Institute of Physics*.

[DOI: 10.1063/1.2722274]

I. INTRODUCTION

Recently, dust has attracted a growing interest as one of critical issues in the next-step fusion tokamak devices mainly for safety reasons because dust can enhance the tritium inventory and the risk of explosion at an accidental air or coolant leakage. Dust also can be an important contributor to impurity contamination of the core and scrape-off-layer (SOL) plasmas in tokamak fusion devices,[1–4] which may increase radiation loss from the plasmas and affect recycling regimes in the divertor regions. Thus, novel experimental and theoretical studies[1–19] on dust composition; mechanisms of dust formation; dust thermochemical, electrical, magnetic and radiative properties; statistical distribution of dust particles over sizes, shapes, porosity, etc.; and dust transport in fusion plasma devices have started. For example, mechanisms of carbon dust formation in divertor simulation experiments have been investigated by Ohno *et al.*[15] showing that the redeposition process of hydrocarbon ions due to pronounced plasma flow is one of the key factors determining dust growth as well as chemical sputtering. The transport of carbon dust particles in tokamak edge plasmas has been studied by Krasheninnikov *et al.*[7] and by Pigarov *et al.* using the numerical simulation approach.[1–3] In particular, these simulations demonstrated the large mobility of dust particles in various plasmas, predicted rather deep penetration of dust particles toward the core plasma in the current tokamaks, and pointed out the potential importance of dust transport for plasma performance in the next-step fusion devices. Work on validation of dust simulation codes against experiments on fusion devices has begun.[5,6]

At present, various materials are used for the plasma facing components (such as chamber wall tiles, divertor plates, limiters, antennae, etc.) in various fusion devices, including tokamaks and stellarators. Different materials (and combination of materials) are considered in attempt to reduce the destruction rate of plasma facing surfaces and to suppress the contamination of plasma with heavy impurities. Table I lists the materials used for plasma facing components (PFC) in different fusion devices around the world and in ITER.[20–39] As seen, the commonly used materials are Be, C, Fe, Mo, and W. The choice of material in current devices is typically governed by specific thermochemical characteristics in hydrogen plasma environment, cost, and suitable construction properties as well as by plasma performance considerations. Note that boron was widely used in recent fusion plasma experiments as the restorable coating of PFCs. All these elements are found to form the dust particles collected and analyzed from the interiors of tokamaks[16] and stellarators.[17] Lithium is considered as one of basic materials in the liquid first wall concept.[40,41]

Injection of dust particles has been proposed as a tool for plasma diagnostics. In Ref. 18, a hypervelocity dust beam injector was considered for internal magnetic field mapping and various materials were suggested (Li, Al, and C). The model for calculating the penetration of a hypervelocity dust beam into the plasma including dust charging and heating by plasma was recently developed in Ref. 19. The analysis based on a high-speed multiview camera system can be used for plasma flow measurements in the scrape-off layer and divertor regions of tokamaks.

Various characteristics of materials listed in Table I, such as phase transition temperatures, specific-heat capacity, and chemical, optical, magnetic, and electrical properties, can af-

---

[a)] Author to whom correspondence should be addressed. Electronic mail: tanaka@ec.t.kanazawa-u.ac.jp

TABLE I. Materials used for plasma facing wall and divertor/limiter in fusion devices (Refs. 20–22).

Device	Plasma facing material	Divertor/Limiter	References
Alcator C-Mod	Mo	Mo	23
ASDEX	SUS	C, W	24
DIII-D	Graphite	ATJ graphite	25
EXTRAP-T2R	SUS	Mo	26
HT-7U	SUS	Graphite	27
(ITER	Be	C, W	28
JET		C, Be	29
JT-60U	Graphite	CFC	30
LHD	SUS316	Graphite	31
MST	Aluminum	10% graphite coverage	32
NSTX	Graphite	Graphite	33
TORE SUPRA	SUS	W	34
TPE-RX	SUS316L	Mo	35
TRIAM-1M	SUS304L	Mo	36
TJ-II	SUS	Graphite	37
W7AS	SUS/Cu	Graphite	38
W7X	Boron carbide	Graphite	39

fect the dynamics of dust particles in tokamak plasmas. While the dynamics of dust particles[1–7] and statistically averaged macroscopic dust profiles[2,3] in tokamak plasmas are intensively studied for carbon, the behavior of dust consisting of other fusion-related materials or of a combination of materials remains unexplored.

In this paper, we consider the behavior of dust particles consisting of major fusion materials (namely Li, Be, B, C, Fe, Mo, and W) in the tokamak plasmas by using numerical simulations with the dust transport code DUSTT.[1] The DUSTT physical model modified to simulate different materials will be discussed in Sec. II. In this section, we also compare some thermochemical properties of the listed materials. In Sec. III, the temporal evolution of dust temperature and mass is simulated for the dust particle in the uniform plasma with parameters typical for tokamak divertors. The dependencies of dust survival time on plasma parameters are presented for different dust materials. The comparative analysis of dust lifetimes will be given. In Sec. IV, we study the dynamics of dust particles for different materials in the edge plasma of the DIII-D tokamak. The effect of dust material on the acceleration, heating, and evaporation/sublimation of dust particles will be analyzed. Conclusions will be given in Sec. V.

II. MODELING OF DUST TRANSPORT FOR DIFFERENT MATERIALS WITH THE MODIFIED DUSTT CODE

A. Governing equations of dust transport for different material

The dynamics of dust in fusion devices is strongly coupled with thermochemical, electrical, and optical properties of dust particle material. These properties govern the heating, charging, erosion, and evaporation/sublimation of dust particles in plasmas. The mass of the dust particle also strongly affects the acceleration by the drag force due to dust collisions with plasma ions.

In calculations of dust lifetimes in plasma and in modeling of dust trajectories, we use the DUSTT code.[1] At present, DUSTT takes into account the dust charging due to absorption and neutralization of plasma particles incident on the dust surface as well as the thermionic and secondary electron emission from the surface. The code simulates the ablation of dust particles due to thermal evaporation/sublimation and various sputtering processes.[2] (Note, the DUSTT code is multispecies; it includes processes of backscattering, absorption, and capture of various atomic particles on the dust surface, so that, in modeling, dust particles can grow from net deposition in the impure low-temperature plasmas.[2]) The calculated heat balance of dust includes heating by plasma particles and cooling due to thermal radiation, electron emission, and ablation. The DUSTT code solves a system of coupled equations for the temporal evolution of temperature, charge, mass, and the trajectory of dust particles in the realistic geometry and plasma conditions of tokamaks. The profiles of multispecies plasma and neutral gas in the tokamak edge plasmas were simulated with the transport code UEDGE[42] under assumptions that cross-field plasma transport is anomalous, diffusive/convective, and ballooning-like.[43,44] In UEDGE modeling, anomalous transport coefficients were adjusted to match experimental profile data on tokamaks.[43,44]

In the present paper, we describe further modifications of the DUSTT code to treat the behavior of dust particles of different materials including transitions between the phase states and the temperature-dependent thermochemical properties (the sputtering yields, saturated vapor pressure, specific-heat capacity, and latent heats of melting and evaporation), as well as the physical parameters of different materials, such as the work function, the coefficient of secondary electron emission, complex dielectric function, etc. The modified DUSTT code solves the following equations to simulate dust transport with solid-liquid phase transition. Equation of motion:

$$M_d \frac{d\boldsymbol{v}_d}{dt} = \zeta_{if}(\boldsymbol{F}_c + \boldsymbol{F}_o) + \zeta_{af}\boldsymbol{F}_a - eZ_d\boldsymbol{E} + M_d\boldsymbol{g}. \tag{1}$$

Energy equation:

$$\frac{d}{dt}(M_d c_{pd} T_d) = P_h - P_c \quad (T_d < T_m - \Delta T, T_m + \Delta T < T_d), \tag{2}$$

$$\frac{d}{dt}(M_d H_m \eta_\ell) = P_h - P_c \quad (T_m - \Delta T \le T_d \le T_m + \Delta T). \tag{3}$$

Mass equation:

$$\frac{dM_d}{dt} = 4\pi r_d^2 m_{\mathrm{imp}}(\Gamma_{\mathrm{imp,in}} - \Gamma_{\mathrm{imp,out}}). \tag{4}$$

Here M_d is the mass of dust particle ($=\frac{4}{3}\pi r_d^3 \rho_d$, ρ_d is the mass density of the dust material), $\boldsymbol{v}_d$ is the velocity of the dust particle, $\boldsymbol{F}_c$ is the drag force due to direct ion collection by the dust particle, $\boldsymbol{F}_o$ is the orbital drag force due to ion scattering by the dust particle, $\boldsymbol{F}_a$ is the friction force on the dust particle by neutral atoms, e is the elementary charge, Z_d is the charge number of the dust particle, $\boldsymbol{E}$ is the electric field, $\boldsymbol{g}$ is the acceleration by the gravity, and ζ_{if} and ζ_{af} are the coefficients describing the uncertainty in force values arising from the dust particle shape. In Eqs. (2) and (3), $c_{pd}(T)$ is the specific-heat capacity of the material of the dust particle, T_d is the temperature of the dust particle, η_ℓ is the liquid mass fraction of the dust particle, H_m is the latent heat of melting, T_m is the melting temperature of the dust, ΔT is the temperature range in which dust melting occurs ($\Delta T \ll T_m$, it is introduced for robust implementation of melting and crystallization conditions in the DUSTT code), P_h is the total heating power onto the dust, and P_c is the total cooling power. In Eq. (4), r_d is the radius of the dust particle, m_{imp} is the mass of dust material atom, $\Gamma_{\text{imp,out}}$ is the flux from the dust due to ablation, and $\Gamma_{\text{imp,in}}$ is the adsorbed impurity atom and ion flux onto the dust from the plasma. The main modification in the DUSTT code is the implementation of the melting and crystallization phenomena, as is described by Eq. (3), that is solved, respectively, for positive and negative values of the right-hand side of the equation.

The basic simplified assumptions used in DUSTT are as follows: (i) the dust particle is spherical and it is comprised of uniform matter; (ii) the dust particle is composed of the single material denoted by the corresponding symbol from the periodic table of chemical elements, (iii) thermochemical properties of the dust particle are the same as the properties of material from which this particle is comprised, and (iv) temperature distribution is uniform inside the particle.

The assumption (iv) is valid because the characteristic time for heat conduction inside the dust particle, $\tau_{\text{cond}} = r_d^2 \rho_d c_p / \kappa_d$, where κ_d is the thermal conductivity of the dust material, can be estimated to be less than $\sim 10^{-7}$ s for $r_d = 1.0\ \mu\text{m}$ for any material considered in this paper. This time is several orders of magnitude smaller than the typical dust transport time $\sim 10^{-3}$ s. In addition, in this case the travel distance of the dust particle $v_d \tau_{\text{cond}}$ for a typical velocity v_d of 100 m/s is only 10^{-3} cm, so that the particle almost stays in place in τ_{cond}. Thus, we can assume the uniform temperature distribution inside the dust particle.

The dust particle can lose its mass due to various processes. The DUSTT code model includes the physical and chemical sputtering by ions and atoms, the radiation enhanced sublimation (RES), and the thermal evaporation/sublimation in the dust mass equation (4) as follows:

$$\Gamma_{\text{imp,out}} = \Gamma_{\text{ps}} + \Gamma_{\text{cs}} + \Gamma_{\text{RES}} + \Gamma_{\text{evap}}, \tag{5}$$

where Γ_{ps}, Γ_{cs}, Γ_{RES}, and Γ_{evap} are the ejected fluxes of atoms from a dust particle due to the physical sputtering, the chemical sputtering, RES, and the thermal evaporation/sublimation, respectively. We used semiempirical expressions to describe the dependence of reflection coefficients and physical and chemical sputtering yields on incident energy and angles for different projectile particles and target materials and target temperatures.[45–47] The reflection and sputtering data were numerically averaged over the Maxwellian velocity distribution function of plasma projectile particles. For RES, we have implemented the expressions obtained from adatom evaporation theory fitting the experimental data.[48,49]

The total heating power P_h taken into account in the DUSTT code includes the kinetic energy transfer due to collisions with ions, $P_{\text{kin},i}$, neutral atoms, $P_{\text{kin},a}$, and electrons, $P_{\text{kin},e}$, and the potential energy transfer from collisions with ions P_{pot} as

$$P_h = P_{\text{kin},i} + P_{\text{kin},a} + P_{\text{kin},e} + P_{\text{pot}}. \tag{6}$$

On the other hand, the total cooling power P_c is composed of the thermal radiation power (P_{rad}), the total kinetic power of ejected atoms, molecules, and clusters due to the physical (P_{ps}) and chemical (P_{cs}) sputtering, RES (P_{RES}), the thermal sublimation/evaporation (P_{evap}), and the power of electrons ($P_{e\text{-emit}}$) due to secondary and thermionic electron emission,

$$P_c = P_{\text{rad}} + P_{\text{ps}} + P_{\text{cs}} + P_{\text{RES}} + P_{\text{evap}} + P_{e\text{-emit}}. \tag{7}$$

The details for modeling of the above terms can be found in Refs. 1 and 3. It is important to note that DUSTT takes into account the reduction of thermal radiation from dust particles, the size of which is smaller than the emission wavelength, as described in Ref. 3. In addition, the DUSTT code also solves the equilibrium relation for electric current to obtain the floating potential and the charge number of the dust,

$$\Gamma_e = \Gamma_i + \Gamma_e^{\text{TE}} + \Gamma_e^{\text{SEE}}, \tag{8}$$

where Γ_e and Γ_i are the electron and ion fluxes, respectively, Γ_e^{TE} is the thermionic electron emission flux, and Γ_e^{SEE} is the secondary electron emission flux. The plasma particle (Γ_e and Γ_i) and heat ($P_{\text{kin},i}$, $P_{\text{kin},a}$, $P_{\text{kin},e}$, and P_{pot}) fluxes are obtained according to the orbital motion limited (OML) theory,[50] and the summary of formulas used in DUSTT is given in Ref. 3. The secondary electron emission yield depends on the energy and angles of incident plasma electrons and Γ_e^{SEE} was calculated by its averaging over the velocity distribution function. The secondary and thermionic electron emission fluxes for a positively charged dust particle were modified according to Ref. 51 to include the contribution of the space charge. The thermionic electron emission affects the dust floating potential to be positive when the dust temperature increases to about 3000 K.[8] For B, C, Mo, and W, the thermionic electron emission markedly affects the dust floating potential because the evaporation temperature of these dusts is higher than 3000 K as described later. The secondary electron emission is needed to be considered especially for Li and B, because these materials have very high emission rates at relatively low incident electron energies.

B. Material functions and thermochemical properties

The dynamics of dust particles composed of different materials is affected by differences in material functions and the thermochemical properties. Table II summarizes the material functions for Li, Be, B, C, Fe, Mo, and W used in the present calculation.[52] We used available values of the func-

TABLE II. Physical properties of different amorphous materials (Ref. [52]).

Element	$_3$Li	$_4$Be	$_5$B	$_6$C	$_{26}$Fe	$_{42}$Mo	$_{74}$W
Atomic mass (amu)	6.49	9.01	10.81	12.01	55.85	95.94	183.85
Melting temperature (K)	453.5	1150	1750	–	1200	2150	2450
Latent heat for melting (eV)	0.031	0.161	0.507	–	0.097	0.43	0.486
Latent heat for evaporation (eV)	1.63	3.32	5.75	7.37[a]	4.28	6.81	8.81
Work function (eV)	2.38	3.92	4.50	4.71	4.31	4.30	4.54

[a] Sublimation.

tions for amorphous materials to describe dust properties, as the scanning electron microscope (SEM) observations reveal that the dust collected in fusion experiments has an amorphous structure.[15] Note that materials in amorphous structure have lower melting temperature, latent heat for melting.[52] As seen, lithium has the lowest atomic mass, melting temperature, latent heats of melting and evaporation, and work function among all materials in the table. On the contrary, tungsten has the highest atomic mass, melting temperature, and latent heat of melting and evaporation. This apparently suggests that dust particles composed of heavy materials have the potential to survive longer in the tokamak plasmas. Carbon materials do not have a liquid phase, and thus the phase-transition equation (3) is not solved for carbon dust particles.

Figure 1 shows the dependence of the specific-heat capacity per unit volume, $\rho_d c_{pd}$, on temperature in the range of 400–5000 K for different materials used in this paper. The specific-heat capacity in J/(cm^3 K) was calculated using the temperature-dependent specific heat c_{pd} in J/(mol K) obtained from the JANAF thermochemical tables[52] and the temperature-dependent mass density, ρ_d, of the corresponding materials. The specific-heat capacity determines the heating rate and the range for temperature variation of dust particles embedded into plasma until evaporation. As seen in Fig. 1, the heat capacity of Li is the lowest. On the contrary, Be, B, and Fe have relatively higher values of capacitance among the given materials at temperatures above 500 K, while that of C is moderate. Therefore, the heating rates of dust particles consisting of heavy materials are not always lower than the rates for the lighter ones. Notice, dust particles with larger mass will experience slower acceleration by plasma ions, so that heavy dust particles can more easily attain the thermal equilibrium with local plasma heating and charging.

Figure 2 displays the saturated vapor pressure as a function of temperature for the materials considered in the paper. This pressure determines the temperature and the rate of thermal sublimation/evaporation for dust particles.[1,3] As can be seen, it is considered that the evaporation temperature of Li is the lowest and that of W is the highest. As is shown later in this paper, the thermal evaporation/sublimation appears to be the dominant process for mass loss of dust particles. Therefore, the lower the saturated vapor pressure of the material, the longer is the expected lifetime of a dust particle comprised of this material.

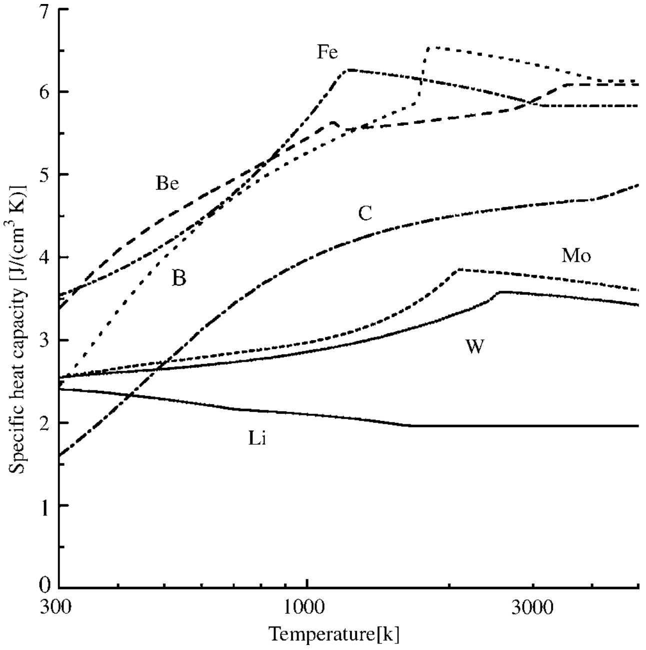

FIG. 1. Specific-heat capacity per unit volume of different amorphous materials.

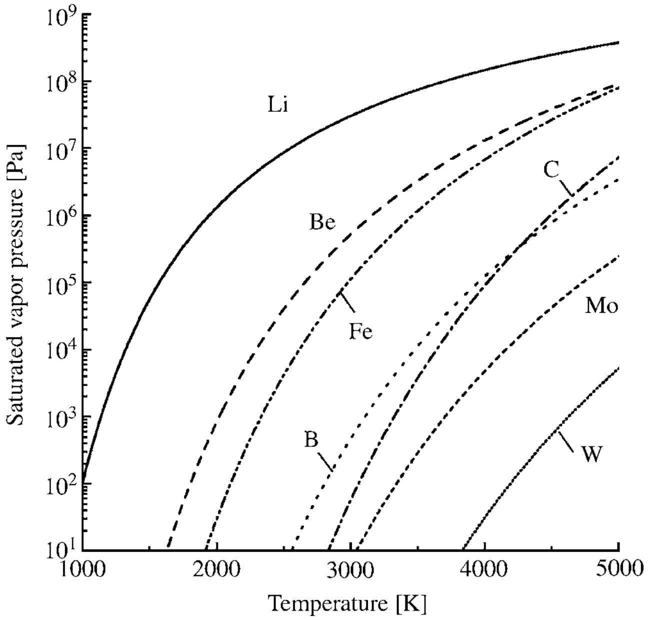

FIG. 2. Saturated vapor pressure of different materials.

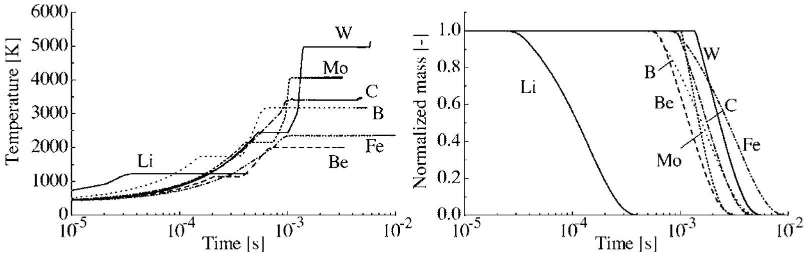

(a) Dust temperature. (b) Mass of dust.

FIG. 3. Temporal evolution of temperature (a) and mass (b) of dust particles for the uniform plasma with parameters: $T_e = T_i = 10$ eV, $T_a = 3$ eV, $n_e = n_i = n_a = 2 \times 10^{13}$ cm^{-3}. Initial dust radius is 1.0 μm.

III. DUST BEHAVIOR IN UNIFORM PLASMAS

A. Calculation conditions

In order to study the effect of the material functions on dynamic behavior of test dust particles, we calculated temporal variations in the dust temperature, potential, radius, and velocity for different materials in the uniform plasma by using the modified DUSTT code. For this study, the values of plasma parameters were selected as follows: $T_i = T_e$, $T_a = 0.3T_i$, $n_e = n_i = n_a$, $|\boldsymbol{E}| = 0$, $|\boldsymbol{g}| = 0$, where T_i, T_e, and T_a are, respectively, the temperatures of ions, electrons, and neutral atoms, and n_i, n_e, and n_a are the density of ions, electrons, and neutral atoms, respectively. The background plasma is assumed to be a deuterium plasma without any impurities. In this case, we set $\Gamma_{\text{imp,in}} = 0$, which means that no deposition occurs onto the dust during its travel in the plasma. The ion flow velocity was set at 10% of the sound speed of ions, i.e., $v_i = 0.1\sqrt{(T_i + T_e)/m_i}$, whereas dust particles were assumed initially immobile in the laboratory system of coordinates. Note that (i) the dust velocity, $\boldsymbol{v}_d$, in the equation of motion (1) is in the laboratory frame, while the ion and neutral drag forces depend on the relative dust-plasma velocity, and (ii) the plasma particle and heat fluxes on dust surface are also dependent on relative velocity. Therefore, in these calculations, the relative velocity between the dust and the plasma varies in time according to the equation of motion. The shape of the dust is assumed to be a sphere with the initial radius $r_{d0} = 1.0$ μm. We used $\zeta_{if} = 1.0$ and $\zeta_{af} = 1.0$. The dust melting temperature range ΔT in Eqs. (2) and (3) was set equal to 1.0 K. The dust dynamics equations (1)–(4) were solved by the first-order explicit Euler method with automatic corrections for time step. The calculations were terminated when the dust radius has become less than 0.01 μm.

B. Temporal evolution of dust temperature and mass

Figures 3(a) and 3(b) show, respectively, the temporal evolutions of the dust temperature and of the ratio of the dust mass to the initial mass for different materials in the uniform plasma with parameters, $T_e = T_i = 10$ eV, $T_a = 3.0$ eV, $n_i = n_e = n_a = 2.0 \times 10^{13}$ cm^{-3}, typical for tokamak edge. As seen, one can distinguish the following four consecutive stages in the dust temperature evolution: (i) initial ramp up in the dust temperature; (ii) dust melting phase at constant temperature; (iii) transition to the thermal equilibrium state; (iv) dust evaporation at thermal equilibrium. Consider, for example, the curves corresponding to the B dust. At the first stage, the dust temperature increases gradually up to the melting point in $t = 0.16$ ms. At the second stage, from $t = 0.16$ to 0.38 ms, the dust temperature has a constant value at 1750 K corresponding to the melting process of the amorphous boron.

From $t = 0.38$ to 0.64 ms, during the third stage, the temperature of the molten dust particle continues to increase. The thermal radiation and other power losses by the dust particle increase substantially reaching the input plasma power level. At these stages, the mass of the B dust is practically not changed as seen in Fig. 3(b). At the last stage, which starts at about $t = 0.64$ ms, the dust temperature attains a constant value at about 3162 K that is an equilibrium temperature determined by the energy balance mainly between the output power flux due to evaporation and radiation and the heating power flux onto the dust from the plasma. The equilibrium becomes possible because input and output power fluxes are both proportional to the dust surface area, while the radius (and the mass) of the B dust decreases rapidly until complete evaporation at 5.3 ms as seen in Fig. 3(b). Note that in the case of carbon dust, there is no melting phase, and thereby stages (i) and (ii) are merged in the one stage.

In Fig. 3, we compare the temporal evolutions of the dust temperature and the dust mass for different materials. As seen, the rate of the increase in dust temperature during the ramp up stage of the Fe dust is the lowest among the materials of interest. Contrarily, the temperature of the Li dust increases much faster in comparison with the other materials. This difference in the temperature increase rate is attributed mainly to the magnitude of the specific-heat capacity of the corresponding materials (see Fig. 1), because dust cooling due to thermal radiation and ablation is negligible at this phase. The dust temperature increase rate at the third stage is also influenced by the specific-heat capacity per unit volume $\rho_d c_{pd}$ according to Eq. (2). The Li dust has the lowest specific-heat capacity, which causes the most rapid temperature increase. At the same time, the Fe dust has the highest specific-heat capacity for temperatures 800–1700 K, which causes the slowest temperature ramp up. Because of low melting temperature, it takes only 0.017 ms for the ramp up stage and about 0.42 ms for all four stages of temperature evolution for the Li dust. In contrast, the evaporation of dust particles made of other materials takes almost an order of magnitude longer time. Notice that dust particles consisting of materials that evaporate at the high equilibrium temperatures (i.e., at temperatures when radiation power loss is significant) exhibit a sharp increase in the temperature shortly before the complete dust destruction, especially for C and W. This final temperature rise is associated with a strong reduction of thermal radiation emissivity for small particles.[3]

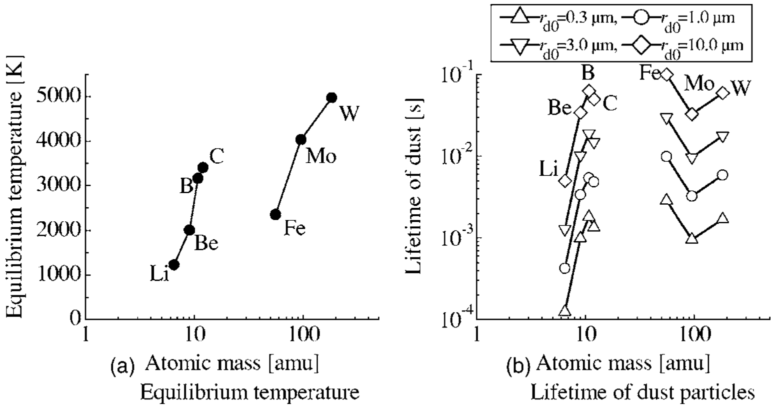

(a) Equilibrium temperature

(b) Lifetime of dust particles

FIG. 4. Equilibrium temperature (a) and lifetime (b) of dust particles for the uniform plasma with parameters: $T_e = T_i = 10$ eV, $T_a = 3$ eV, $n_e = n_i = n_a = 2 \times 10^{13}$ cm^{-3}. The initial dust radius r_{d0} is changed from 0.3 to 10 μm.

The rate of the dust mass decrease at the fourth stage of temperature evolution can be determined by the mass and energy balance equations (2) and (4) rewritten as

$$\frac{dM_d}{dt} c_{pd} T_d + M_d c_{pd} \frac{dT_d}{dt} = 4\pi r_d^2 [q_h - q_{\mathrm{rad}}(T_d) - (2kT_d + H_v)\Gamma_{\mathrm{evap}}(T_d)], \qquad (9)$$

$$\frac{dM_d}{dt} = -4\pi r_d^2 m_{\mathrm{imp}} \Gamma_{\mathrm{evap}}(T_d), \qquad (10)$$

where $q_h = P_h/(4\pi r_d^2)$ is the heating plasma power density per unit area onto the dust particle, $q_{\mathrm{rad}} = P_{\mathrm{rad}}/(4\pi r_d^2)$ is the thermal radiation cooling per unit area, H_v is the latent heat of vaporization, and k is the Boltzmann constant. Here we neglected with cooling mechanisms other than thermal radiation and evaporation in Eq. (9) because the radiation and evaporation terms are the dominant cooling processes during evaporation. The equilibrium dust temperature T_{evap} established at the evaporation process can be found from Eqs. (9) and (10) and the equilibrium condition $dT_d/dt = 0$. Assuming that the heating power is independent on the dust radius and temperature, we get an algebraic equation to determine T_{evap},

$$[H_v + (2k - m_{\mathrm{imp}} c_{pd}) T_{\mathrm{evap}}] \Gamma_{\mathrm{evap}}(T_{\mathrm{evap}}) = q_h - q_{\mathrm{rad}}(T_{\mathrm{evap}}). \qquad (11)$$

Note that $\Gamma_{\mathrm{evap}}(T_d)$ is linearly related with the saturated vapor pressure.

From this consideration, the equilibrium temperature T_{evap} is determined mainly by the saturated vapor pressure, thermal radiation, and the latent heat for evaporation and the heating power q_h. The heating power q_h depends on dust materials if the background plasma is the same, because q_h depends on the floating potential of the dust and the relative velocity between the plasma and the dust. The floating potential of the dust is much influenced by the characteristics on the electron emission of materials. For example, Li and B have high rates of secondary electron emission at the lower incident electron energy, which makes the dust potential positive. The thermionic electron emission is the dominant one for B, C, Mo, and W in order to make the dust potential positive. The more positive potential causes the higher electron flux onto the dust, and then the higher heating power.[3]

Then, from Eqs. (10) and (11), the rate of the dust mass decrease can be written as follows:

$$\begin{aligned} \frac{1}{M_{d0}} \frac{dM_d}{dt} &= -\frac{4\pi r_d^2 m_{\mathrm{imp}}}{M_{d0}} \Gamma_{\mathrm{evap}}(T_{\mathrm{evap}}) \\ &= -\frac{3m_{\mathrm{imp}}}{\rho_{d0} r_{d0}} \left(\frac{r_d}{r_{d0}}\right)^2 \Gamma_{\mathrm{evap}}(T_{\mathrm{evap}}) \\ &= -\frac{3m_{\mathrm{imp}}}{\rho_{d0} r_{d0}} \left(\frac{r_d}{r_{d0}}\right)^2 \frac{q_h - q_{\mathrm{rad}}(T_{\mathrm{evap}})}{H_v + (2k - m_{\mathrm{imp}} c_{pd}) T_{\mathrm{evap}}}, \end{aligned} \qquad (12)$$

where $M_{d0} = \frac{4}{3}\pi r_{d0}^3 \rho_{d0}$ is the initial mass of the dust, and r_{d0} and ρ_{d0} are the initial dust radius and initial mass density, respectively. As one may expect, the destruction rate directly increases with the evaporation flux at the equilibrium temperature $\Gamma_{\mathrm{evap}}(T_{\mathrm{evap}})$, which is proportional to the heating power q_h. The q_h depends on the dust potential (see Ref. 3). Especially for C, Mo, and W, the dust potential changes from negative to positive or zero due to thermionic electron emission because the evaporation temperatures for C, Mo, and W are high (more than 3000 K). It is noted again that this positive potential increases the heating power from the electron flux remarkably.[3]

It also can be seen from Eq. (12) that the dust destruction rate is higher when $m_{\mathrm{imp}}/\rho_{d0}$ and $m_{\mathrm{imp}} c_{pd}$ are large and when H_v is small. Note that $q_{\mathrm{rad}}(T_d)$ is an increasing function of T_d. A combination of these parameters for different materials determines the dust lifetime in the plasma at the final stage of temperature evolution.

Figures 4(a) and 4(b) indicate the calculated equilibrium temperature T_{evap} and the lifetime of the dust particle versus atomic mass. The initial dust radius r_{d0} is taken as a parameter. As seen, T_{evap} is practically independent of r_{d0} via Eq. (11) for dust $r_{d0} > 100$ nm. Note, however, that for smaller particles the thermal radiation q_{rad} depends on radius. In Fig. 4(a), one can distinguish two characteristic curves of T_{evap} for light elements of Li, Be, B, and C, and for heavy elements Fe, Mo, and W. The equilibrium temperatures T_{evap} for the light elements increase with atomic mass. Another increasing relation with atomic mass can also be found for T_{evap} for heavy elements (such as Fe, Mo, and W) as seen in Fig. 4(b). However, the lifetime does not have a simple de-

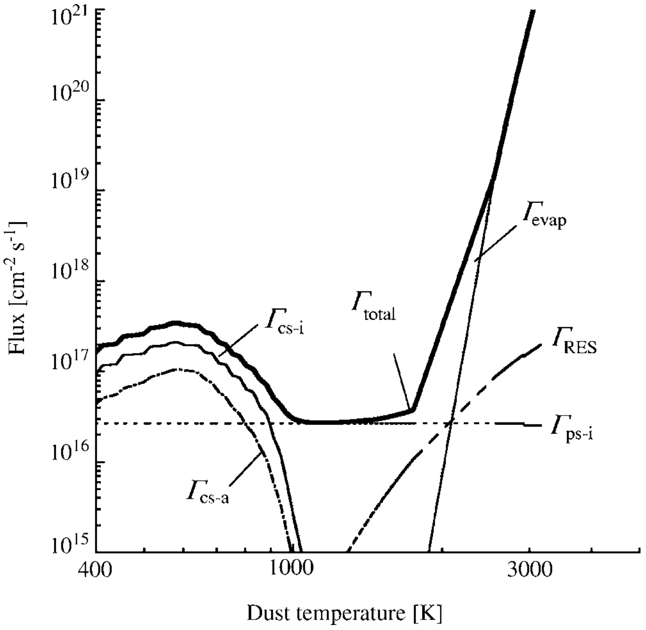

FIG. 5. Ejected flux components from the boron dust. $\Gamma_{\text{cs}-i}$ is the flux due to chemical sputtering with ions, $\Gamma_{\text{cs}-a}$ is the flux due to chemical sputtering with neutral atoms, $\Gamma_{\text{ps}-i}$ is the flux due to physical sputtering with ions, Γ_{res} is the flux due to adatom sublimation, Γ_{evap} is the flux due to thermal evaporation, and Γ_{total} is the total flux from dust. The uniform plasma parameters are $T_e=T_i=10$ eV, $T_a=3$ eV, $n_e=n_i=n_a=2\times10^{13}$ cm^{-3}.

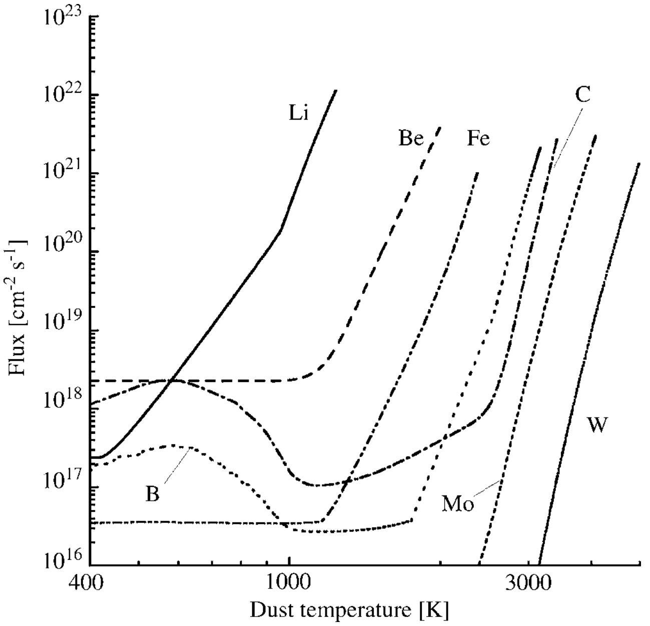

FIG. 6. Total ejected flux from dust made of various materials. Plasma parameters are $T_e=T_i=10$ eV, $T_a=3$ eV, $n_e=n_i=n_a=2\times10^{13}$ cm^{-3}.

pendence on the atomic mass. In this case, Fe has a longer lifetime mainly because of its higher specific-heat capacity and lower equilibrium temperature T_{evap} which causes small ejected flux. At the same time, the lifetime of Mo is shorter than those of Fe and W. This is because Mo has higher ejected flux due to evaporation at its T_{evap} as described later. In addition, the lifetime of all materials is in proportion to the initial dust radius r_{d0}. This is because the characteristic time of the mass decrease is in proportion to $\rho_{d0}r_{d0}/[m_{\text{imp}}\Gamma_{\text{evap}}(T_{\text{evap}})]$ for $r_d/r_{d0}=0.01$ from Eq. (12). The T_{evap} is independent of r_{d0}. Thus, the characteristic time of the mass decrease, which determines the lifetime, is proportional to $\rho_{d0}r_{d0}/m_{\text{imp}}$.

C. Mass loss processes for dust particles made of different materials

To find the dominant processes of dust mass loss, we calculated the fluxes ejected from the dust due to each of the contributing processes: physical and chemical sputtering, radiation enhanced, and thermal sublimation/evaporation. Figure 5 displays the ejected fluxes from the B dust versus the dust temperature at the given plasma parameters, $T_e=T_i=10$ eV, $T_a=3.0$ eV, $n_i=n_e=n_a=2.0\times10^{13}$ cm^{-3}, as an example. In this figure, one can see that the chemical sputtering by ions is the dominant process for the mass loss at dust temperatures below 1000K in the considered plasma.

From 1000 to 2000 K, the physical sputtering is found to be the main process for the mass loss, but the associated sputtered flux is smaller than that at temperatures below 1000 K. The magnitude of the both ejected fluxes is less than 10^{18} cm^{-2} s^{-1} for the given background plasma conditions. In the range from 2000 to 3200 K, the ejected flux drastically increases with the dust temperature. Around this temperature, the adatom sublimation and thermal evaporation occur. In particular, the ejected flux due to the thermal evaporation remarkably increases with the dust temperature, reaching the 10^{21} cm^{-2} s^{-1} level at 3000 K. As seen, the thermal evaporation is the dominant process for mass loss of the dust in plasma.

The similar picture of dust mass evolution was obtained for other materials. Figure 6 shows the total ejected flux from the dust particles of different materials in the temperature range from 400 K to the equilibrium temperature T_{evap} corresponding to each material. As seen, for the B and C dusts, the chemical sputtering plays an important role in the mass reduction at low temperatures below 1000 K. The chemical sputtering does not occur for the other materials (Li, Fe, Mo, W), as they do not produce molecules with deuterium. At the same time, for any materials, the substantial ejected flux is attributed mainly to the thermal evaporation/sublimation. It should be noted that the largest points on each of the curves in Fig. 6 indicate the flux ejected during the dust evaporation phase for corresponding material. Comparing these points, it can be seen that Li has the largest ejected flux during its evaporation, while that of Fe is the least. The magnitude of the ejected fluxes can explain the difference in the rate of dust mass loss for different materials in Fig. 3(b).

D. Lifetime of dust made of different materials

The lifetime is one of the most important characteristics of dust particle dynamics in fusion plasmas. The lifetime may depend strongly on many parameters describing (i) material functions such as specific heat and saturated vapor pressure, (ii) some complex dust-plasma interaction phenomena leading to mass loss, and (iii) electron and radiation emission properties; as has been described in the previous

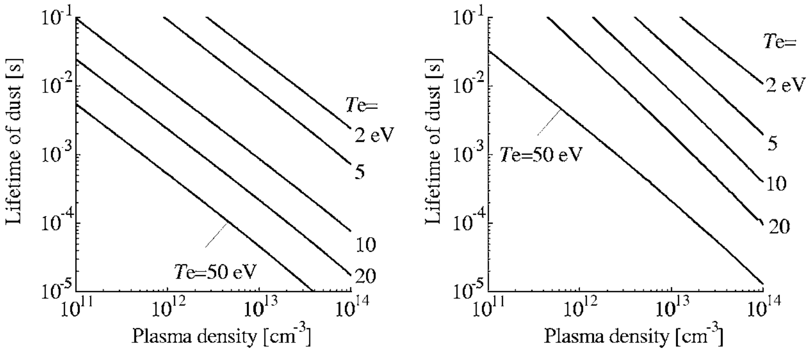

(a) Lithium (b) Beryllium

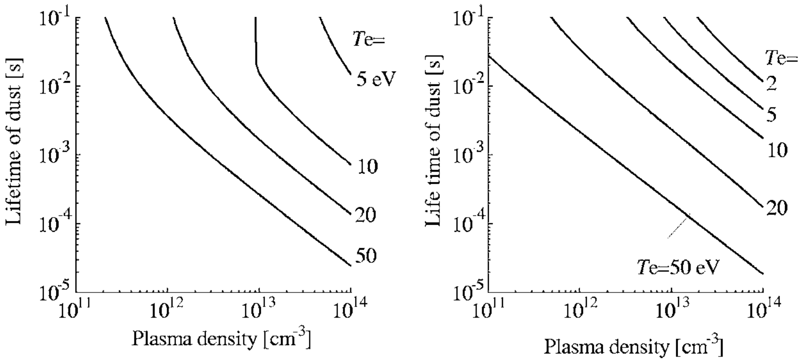

(c) Carbon (d) Iron

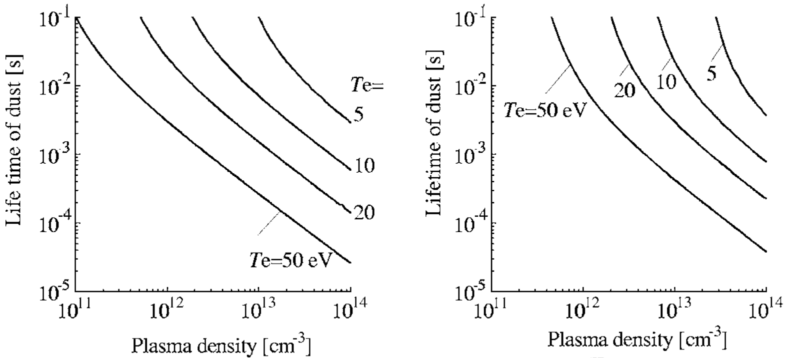

(e) Molybdenum (f) Tungsten

FIG. 7. Lifetime of dust particles displayed for different materials as functions of plasma density and temperature. Plasma parameters are $T_i = T_e$, $T_a = 0.3T_i$, $n_e = n_i = n_a$. Initial dust radius is 1.0 μm.

section. The dust charge number or floating potential can also affect the lifetime because they markedly influence the ion and electron fluxes onto the dust, $P_{\mathrm{kin},i}$ and $P_{\mathrm{kin},e}$. Here we present the results of DUSTT calculations for the lifetime of dust particles made of different materials in various uniform plasmas.

The lifetimes for Li, Be, C, Fe, Mo, and W dust particles are displayed as functions of plasma density n_e and temperature T_e in Fig. 7 in panels (a)–(f), respectively. The curves are plotted for plasma density in the range of $10^{11}-10^{14}$ cm^{-3} and for a set of different electron temperatures in the range of 2–50 eV that are typical for tokamak edge plasmas. As seen in all the panels, when T_e and n_e increase, the dust lifetime monotonically decreases mainly because of the greater energy flux onto the dust, which increases the dust temperature and intensifies the dust ablation. For Li dust particles [panel (a)], the lifetime dependence on plasma density can be well fitted by n_e^{-1} law at fixed T_e. As follows from a comparison of panels in Fig. 7, the lifetimes of Be, C, Fe, Mo, and W dusts are much longer than the Li dust lifetime for the same plasma parameters. For Be dust, one can fit the lifetime dependencies on the plasma density by power law $n_e^{-\alpha}$, where α is the positive number weakly dependent on T_e and whose best fit is $\alpha = 1.26$ for $T_e = 10$ eV. For other materials, C, Fe, Mo, and W, the lifetime curves are nonlinear functions of both T_e and n_e. Particularly for C dust at $T_e = 10$ eV, the lifetime sharply increases from 0.023 to 0.12 s as the plasma density n_e decreases a bit from 9.3×10^{12} to 8.7×10^{12} cm^{-3}.

The lifetime of dust of different materials is plotted in Fig. 8(a) as a function of plasma density n_e in the background plasma with fixed temperature values: $T_i = T_e = 10$ eV and $T_a = 3.0$ eV. It is clearly seen from this figure that the lifetime of Li is much shorter than lifetimes of other materials at any n_e. The presented dust materials have different dependencies of their lifetime on plasma density. For example, the lifetime of Mo and Be is relatively shorter in the wide range of n_e from 0.3×10^{13} to 2×10^{13} cm^{-3} than

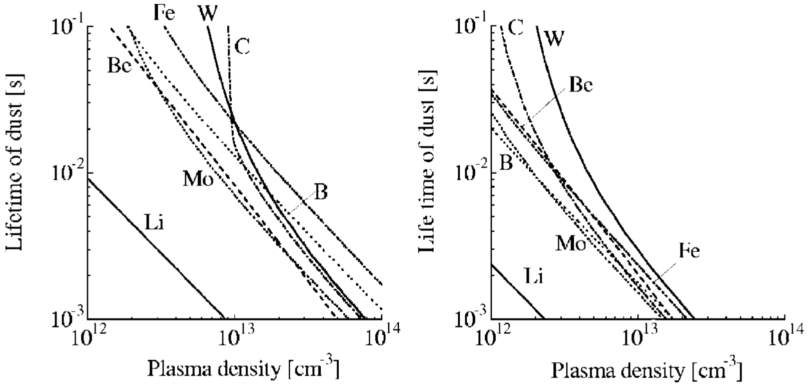

(a) $T_e = T_i = 10$ eV.

(b) $T_e = T_i = 20$ eV.

FIG. 8. Lifetime of dust particles versus plasma density at (a) $T_i = T_e = 10$ eV and $T_a = 3$ eV, and (b) $T_i = T_e = 20$ eV and $T_a = 6$ eV for different materials. Initial dust radius r_{d0} is 1.0 μm.

the lifetime of B, C, Fe, and W. This is because Mo and Be have the higher evaporation fluxes as indicated in Fig. 6(a) with respect to other materials. At $n_e > 10^{13}$ cm^{-3}, the Fe dust has the longest lifetime for the given T_e. This can be attributed to the specific combination of its properties: high heat capacity, relatively low evaporation flux, and relatively low evaporation temperature. At the same time, at $n_e < 10^{13}$ cm^{-3}, the lifetime of C and W dusts is longer than the lifetime of the others. This is due to the fact that these materials have relatively small heat capacity and high sublimation temperatures. In this case, dust particles attain lower equilibrium temperature T_{evap}. This lower equilibrium temperature reduces the evaporation flux according to the temperature-dependent saturated vapor pressure, and reduces the heating power related to the negative floating potential. The combination of the above facts makes the lifetime of dust strongly nonlinearly dependent on n_e. Figure 8(b) shows the dust lifetime for different materials in the higher temperature plasma with $T_i = T_e = 20$ eV and $T_a = 6.0$ eV. As seen, in this case, the W dust has the longest lifetime for any n_e. At the same time, the B dust has the relatively short lifetime at $n_e < 10^{13}$ cm^{-3} compared to other materials except Li. So, the lifetime is also strongly nonlinearly dependent on T_e.

Figure 9 shows the dependencies of the lifetime of dust of different materials on T_e in a plasma with fixed $n_e = 2 \times 10^{13}$ cm^{-3}. Although the dependencies are generally decreasing with T_e for all the materials, they have substantially different behavior at low temperatures that depends on the characteristics of sputtering processes. The lifetime of B, C, Mo, and W dusts exhibits a very sharp increase at T_e below 10 eV, while the plasma temperature dependencies for Li, Be, and Fe dusts are more monotonic with moderately sharp changes near the infliction points. The diversity in temperature dependencies causes the different materials to have the longest lifetime in different ranges of T_e. For example, with increasing of T_e from 10 to 20 eV, the Fe dust has the longest lifetime, then the W dust takes the lead from 20 to 50 eV and competes closely with the B dust at the higher temperatures. It is important to note that although there is the large difference in the lifetime between the materials at low plasma temperatures ($T_e < 10$ eV), at higher plasma temperatures the difference in lifetime does not exceed a few times for all considered materials except for Li.

Note that Martin *et al.* had calculated in Ref. 53 the lifetimes of C and W particles in the case of uniform plasma. They indicated that the lifetime of the W dust was much longer than the lifetime of the C dust in the T_e range of 40–100 eV and $n_e = 10^{13}$ cm^{-3}. These results are different from our results obtained with DUSTT code and presented in Fig. 7. The difference is mainly because the authors of Ref. 53 neglected the secondary electron and thermionic electron emission from the dust particles. The secondary and thermionic electron emission efficiently reduces the negative floating potential of dust particles in plasma and even makes it positive, and then markedly increases the plasma heat flux onto the dust surface. This effect drastically changes the dust lifetime for materials with high evaporation/sublimation temperature (such as C, Mo, and W) and, in our present calculation, the effect has strictly been taken into account. In addition, in our model both plasma particles and heat fluxes are calculated self-consistently from the OML theory.[3]

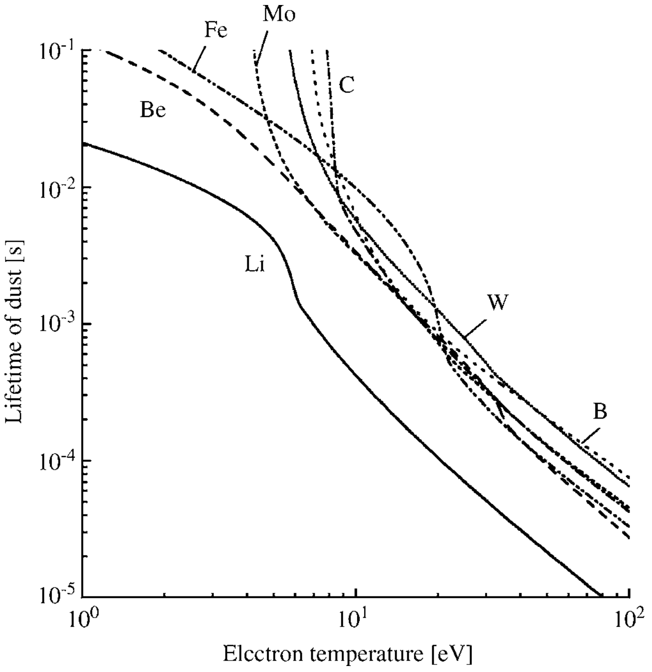

FIG. 9. Temperature dependence of dust lifetime for different materials at plasma density $n_i = n_e = 2 \times 10^{13}$ cm^{-3}. Plasma temperatures are $T_i = T_e$, $T_a = 0.3 T_a$. Initial dust radius r_{d0} is 1.0 μm.

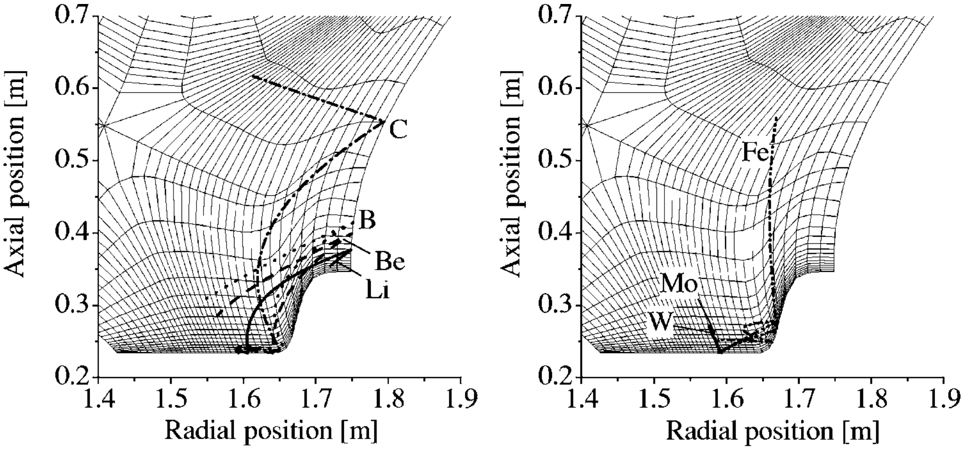

(a) Light materials.

(b) Heavy materials.

FIG. 10. Examples of trajectories for dust made of different materials calculated for DIII-D tokamak plasma. Panel (a) displays trajectories of light particles, whereas trajectories of heavy particles are shown in panel (b).

IV. DUST BEHAVIOR IN TOKAMAK PLASMAS

In order to study the dust dynamics for different materials in tokamaks, we simulated the trajectories of dust particles in the typical L-mode plasma discharge on the DIII-D tokamak (see Ref. 2 for discharge plasma profiles), although it is a carbon-based device. For this calculation, test dust particles of various materials were injected from the strike point on the outer divertor plate toward the core with an initial velocity of 10 m/s. The initial radius of the dust particles was 1.0 μm. The injection direction was set by the angle of 30° to the normal to the divertor plate surface and 45° to the toroidal direction. The profiles of plasma parameters for this DIII-D discharge were computed with plasma transport code UEDGE. The dust collisions with plasma facing material surfaces (divertor plates, chamber walls, limiters) were treated as specular-diffusive reflection. The mirror reflection probability for a solid dust was set to 0.5, and that for a molten dust was set to 0.25. The restitution coefficients[54] for a solid dust and a liquid dust were set to 0.85 and 0.15, respectively.

Figure 10 shows the simulated trajectories of the dust particles of different materials in the poloidal cross section of the DIII-D tokamak device (light elements Li, B, Be, and C are shown in the left panel, whereas heavy elements Fe, Mo, and W are shown in the right panel). As seen, the light dust particles of Li, B, Be, and C are very mobile, easily accelerated by toroidal plasma flow, and experience multiple collisions with the walls. Due to the fast acceleration and the wall collisions, they travel long distances and spread over the divertor region penetrating to the high-density plasma region (we refer the reader to the detailed analysis of dust dynamics in tokamaks given in Refs. 1–3 for carbon particles). Contrarily, heavy dust particles of Mo and W are hardly accelerated by plasma ions and slowly move along almost straight trajectories, because of their large inertia. Due to moving straight (and due to the choice of initial velocity direction toward the plasma core), these dust particles do not collide with the chamber walls and evaporate when they reach a nearest hot and dense plasma region. Such behavior causes shorter travel lengths and less spreading of the Mo and W particles in comparison with the light ones. The Fe dust demonstrates the ability to accelerate due to the long lifetime and the moderate weight.

Figure 11 demonstrates temporal evolution in temperature, mass, and velocity of the test dust particles made of different materials during their motion in the DIII-D tokamak

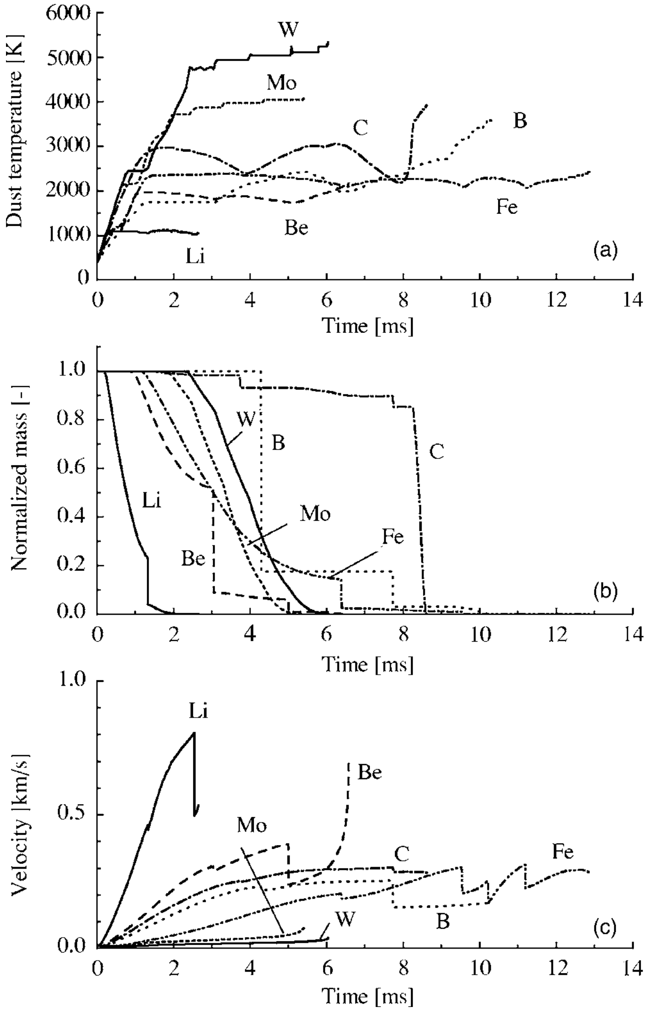

FIG. 11. Temporal variation of temperature (a), mass (b), and velocity (c) of dust particles made of different materials in the DIII-D tokamak.

plasma. The temperature of the dust particles increases quickly as they start their motion at the strike point. After the initial heating, the light particles show nonmonotonic temperature variation in time as they enter or leave the cold plasma regions near the wall due to the collisions. The heavy dust particles have monotonically increasing temperatures with a plateau during the melting process. Melting of the light particles occurs during the initial heating stage at relatively low temperatures. Note that the light particles are not cooled enough during the dust motion to recrystallize. Following their temperature variation, the dust particles lost their mass due to thermal evaporation, and also in wall collisions as indicated in the middle panel of Fig. 11. Especially, dusts in liquid phase markedly lose their mass by collision with the wall, as for Li, Be, B, and Fe. Since C has no liquid phase, it loses its mass mainly by thermal sublimation. In the bottom panel of the figure, we can see the dust velocity evolution during motion in the tokamak. As was shown previously, the dust is accelerated mainly due to the ion drag force.[1] As a result, light dust particles can be easily accelerated to reach several hundred m/s in tokamaks. In contrast, the heavy dust is almost not accelerated until its size is reduced significantly just before complete destruction.

V. CONCLUSIONS

The behavior of dust particles of different materials (Li, Be, B, C, Fe, Mo, and W) in fusion plasmas was simulated by the DUSTT code modified for a variety of materials. The main modification was made to treat the phase transition between solid and liquid states of the dust. The temperature-dependent thermochemical, electric, and thermal radiation properties and other physical functions of the materials were also taken into the account.

The temporal evolution of the dust temperature and dust mass was calculated for uniform plasma conditions. The four stages of dust heating/evaporation were demonstrated, including (i) initial temperature ramp up, (ii) melting, (iii) transition to thermal equilibrium, and (iv) evaporation at the equilibrium temperature. It was shown that the dominant process for reducing the mass of the dust is thermal evaporation/sublimation, which depends on the saturated vapor pressure at the thermal equilibrium temperature.

The lifetime of the dust was estimated for different materials as a function of plasma parameters. It was shown that different materials may have the longest lifetime in different ranges of plasma temperature and density. The presented results can be useful for estimates of penetration length of dust particles made of different materials traveling in fusion devices.

The dynamics of dust particles in nonuniform tokamak plasmas was studied. The difference in the dynamics of particles made of light and heavy materials was demonstrated. Comparing different dust trajectories, we found that C and Fe dust particles can penetrate deeply into the tokamak plasma. Especially among metallic particles, iron dust demonstrates high mobility due to the long lifetime and the moderate weight favorable for rapid acceleration by hydrogenic plasma ions.

Future work will include the DUSTT code simulation and analysis of statistically averaged profiles of dust parameters in tokamak plasmas (see Refs. 2 and 3) for particles made of different materials.

ACKNOWLEDGMENTS

One of the authors (Y.T.) would like to express his appreciation to Dr. N. Asakura, Japan Atomic Energy Agency, for his advice.

This work was partially done according to the Japan–U.S. Collaboration Program in the National Institute of Fusion Science, Japan. The work was supported by the U.S. Department of Energy under Grant No. DE-FG02-04ER54852 at the University of California, San Diego.

[1] A. Yu. Pigarov, S. I. Krasheninnikov, T. K. Soboleva, and T. D. Rognlien, Phys. Plasmas **12**, 122508 (2005).
[2] A. Yu. Pigarov, R. D. Smirnov, S. I. Krasheninnikov, T. D. Rognlien, M. Rosenberg, and T. K. Soboleva, "Transport of dust particles in tokamak devices," J. Nucl. Mater. (in press).
[3] R. D. Smirnov, A. Y. Pigarov, M. Rosenberg, S. I. Krasheninnikov, and D. A. Mendis, Plasma Phys. Controlled Fusion **49**, 347 (2007).
[4] S. I. Krasheninnikov, Y. Tomita, R. D. Smirnov, and R. K. Janev, Phys. Plasmas **11**, 3141 (2004).
[5] A. L. Roquemore, W. Davis, R. Kaita, C. H. Skinner, R. Maqueda, and N. Nishino, Rev. Sci. Instrum. **77**, 10E526 (2006).
[6] A. L. Roquemore, N. Nishino, C. H. Skinner, C. Bush, R. Kaita, R. Maqueda, A. Yu. Pigarov, and S. I. Krasheninnikov, "3D measurements of mobile dust particle trajectories in NSTX," J. Nucl. Mater. (in press).
[7] S. I. Krasheninnikov and T. K. Soboleva, Plasma Phys. Controlled Fusion **47**, A339 (2005).
[8] S. I. Krasheninnikov, A. Yu. Pigarov, Y. Tanaka, I. H. Hutchinson, T. D. Rognlien, and T. K. Soboleva, Contrib. Plasma Phys. **46**, 611 (2006).
[9] J. Winter, Plasma Phys. Controlled Fusion **46**, B583 (2004).
[10] M. Rubel, M. Cecconello, J. A. Malmberg, G. Sergienko, W. Biel, J. R. Drake, A. Hedqvist, A. Huber, and V. Philipps, Nucl. Fusion **41**, 1087 (2001).
[11] L. A. Dorf, A. L. Roquemore, G. A. Wurden, C. M. Ticos, and Z. Wang, Rev. Sci. Instrum. **77**, 10E517 (2006).
[12] J. Winter and G. Gebauer, J. Nucl. Mater. **266–269**, 228 (1999).
[13] G. Federici, C. H. Skinner, J. N. Brooks, J. P. Coad, C. Grisolia, A. A. Haasz, A. Hassanein, V. Philipps, C. S. Pitcher, J. Roth, W. R. Wampler, and D. G. Whyte, Nucl. Fusion **41**, 1967 (2001).
[14] S. Takamura, N. Ohno, D. Nishijima, and Y. Uesugi, Plasma Sources Sci. Technol. **11**, A42 (2002).
[15] N. Ohno, Y. Kobayashi, T. Sugimoto, and S. Takamura, J. Nucl. Mater. **337–339**, 35 (2005).
[16] J. P. Sharpe, P. W. Humrickhouse, C. H. Skinner *et al.*, J. Nucl. Mater. **337–339**, 1000 (2005).
[17] M. Shiratani, S. Kiridoshi, and K. Koga, "Characterization of dust particles ranking in size from 1 nm to over 10 mkm collected from LHD," J. Nucl. Mater. (to be published).
[18] Z. Wang and G. A. Wurden, Rev. Sci. Instrum. **74**, 1887 (2003).
[19] C. M. Ticos, Z. H. Wang, G. L. Delzanno *et al.*, Phys. Plasmas **13**, 103501 (2006).
[20] Fusion Device Database, Data and Planning Center, National Institute for Fusion Science, Japan, http://dpc.nifs.ac.jp/fudev/
[21] G. Federichi, C. H. Skinner, J. N. Brooks, J. P. Coad, C. Grisolia, A. A. Haasz, A. Hassanein, V. Philipps, C. S. Pitcher, J. Roth, W. R. Wampler, and D. G. Whyte, Nucl. Fusion **41**, 1967 (2001).
[22] J. Linke, Phys. Scr., T **T123**, 45 (2006).
[23] I. H. Hutchinson, R. Boivin, F. Bombarda, P. Bonoli, S. Fairfax, C. Fiore, J. Goetz, S. Golovato, R. Granetz, and M. Greenwald, Phys. Plasmas **1**, 1511 (1994).
[24] A. Gude, Nucl. Fusion **42**, 833 (2002).
[25] J. L. Luxon, Nucl. Fusion **42**, 614 (2002).
[26] P. R. Brunsell, Plasma Phys. Controlled Fusion **43**, 1457 (2001).
[27] J. Li, B. N. Wan, and J. S. Mao, Plasma Phys. Controlled Fusion **42**, 135 (2000).
[28] R. Aymar, Plasma Phys. Controlled Fusion **44**, 519 (2002).

[29] P. H. Rebut, Nucl. Fusion **25**, 1011 (1985).
[30] S. Ishida and JT-60 Team, Nucl. Fusion **39**, 1211 (1999).
[31] O. Motojima, K. Akaishi, and H. Chikaraishi, Nucl. Fusion **40**, 599 (2000).
[32] R. N. Dexter, D. W. Kerst, T. W. Lovell, S. C. Prager, and J. C. Stott, Fusion Technol. **19**, 131 (1991).
[33] M. Ono, S. M. Kaye, and Y.-K. M. Peng, Nucl. Fusion **40**, 557 (2000).
[34] M. Chatelier, Phys. Plasmas **8**, 2148 (2001).
[35] Y. Yagi, Plasma Phys. Controlled Fusion **41**, 2552 (1999).
[36] H. Zushi, Nucl. Fusion **43**, 1600 (2003).
[37] C. Alejaldre, J. Alonso, and J. Botija, Fusion Technol. **17**, 131 (1990).
[38] G. Grieger, Phys. Fluids B **4**, 2081 (1992).
[39] J. Nuhrenberg, Trans. Fusion Technol. **27**, 71 (1995).
[40] S. I. Krasheninnikov, L. E. Zakharov, and G. V. Pereverzev, Phys. Plasmas **10**, 1678 (2003).
[41] R. E. Nygen, D. F. Cowgill, M. A. Ulrickson *et al.*, Fusion Eng. Des. **72**, 223 (2004).
[42] T. D. Rognlien, J. L. Milovich, M. E. Rensink, and G. D. Porter, J. Nucl. Mater. **196–198**, 347 (1992).
[43] A. Yu. Pigarov, E. M. Hollmann, S. I. Krasheninnikov, T. D. Rognlien, and W. P. West, J. Nucl. Mater. **337–339**, 371 (2005).
[44] A. Yu. Pigarov, S. I. Krasheninnikov, and B. LaBombard, Contrib. Plasma Phys. **46**, 604 (2006).
[45] W. Eckstein, J. Nucl. Mater. **248**, 1 (1997); E. W. Thomas, R. K. Janev, and J. J. Smith, Nucl. Instrum. Methods Phys. Res. B **69**, 427 (1992); T. Tabada, R. Ito, K. Morita *et al.*, *ibid.* **9**, 113 (1985).
[46] W. Eckstein and R. Preuss, J. Nucl. Mater. **320**, 209 (2003); C. Garcia-Rosales, W. Eckstein, and J. Roth, *ibid.* **218**, 9 (1994); J. Bohdansky, Nucl. Instrum. Methods Phys. Res. B **2**, 587 (1984); N. Matsunami, Y. Yamamura, Y. Itikawa *et al.*, At. Data Nucl. Data Tables **31**, 1 (1984); J. Roth, J. Nucl. Mater. **266–269**, 51 (1999); J. W. Davis and A. A. Haasz, *ibid.* **241–243**, 37 (1997).
[47] J. Roth, E. Vietzke, A. A. Haasz *et al.*, Nucl. Fusion Suppl. **1**, 63 (1991).
[48] R. P. Doerner, S. I. Krasheninnikov, and K. Schmid, J. Appl. Phys. **95**, 4471 (2004).
[49] R. P. Doerner, M. J. Baldwin, S. I. Krasheninnikov, and K. Schmid, J. Nucl. Mater. **337–339**, 877 (2005).
[50] H. M. Mott-Smith and I. Langmuir, Phys. Rev. **28**, 727 (1926).
[51] M. S. Sodha and S. Guha, Adv. Plasma Phys. **4**, 219 (1971).
[52] M. W. Chase, Jr., J. Phys. Chem. Ref. Data Monogr. **9**, 1 (1998).
[53] J. D. Martin, M. Coppins, and G. F. Counsell, J. Nucl. Mater. **337–339**, 114 (2005).
[54] S. I. Krasheninnikov, R. D. Smirnov, D. J. Benson, A. Yu. Pigarov, T. K. Soboleva, T. D. Rognlien, M. Rosenberg, V. I. Shevchenko, P. K. Shukla, and D. A. Mendis, "Modeling of dust-particle dynamics, transport, and impact on tokamak plasma performance," in *Online Proceedings of the 21st IAEA Fusion Energy Conference*, Chengdu, China, 16–21 October 2006 (International Atomic Energy Agency, Vienna, 2006), paper TH/P6-18.